Determining the $CH_3SO_2 \rightarrow CH_3 + SO_2$ barrier from methylsulfonyl chloride photodissociation at 193 nm using velocity map imaging

Britni J. Ratliff,[1] Xiaonan Tang,[1] Laurie J. Butler,[1,a)] David E. Szpunar,[2] and Kai-Chung Lau[3,a)]
[1]*Department of Chemistry and The James Franck Institute, University of Chicago, Chicago, Illinois 60637, USA*
[2]*Department of Biological, Chemical, and Physical Sciences, Roosevelt University, Schaumburg, Illinois 60173, USA*
[3]*Department of Biology and Chemistry, City University of Hong Kong, Hong Kong*

(Received 20 February 2009; accepted 4 June 2009; published online 22 July 2009)

These imaging experiments study the formation of the methylsulfonyl radical, CH_3SO_2, from the photodissociation of CH_3SO_2Cl at 193 nm and determine the energetic barrier for the radical's subsequent dissociation to CH_3+SO_2. We first state-selectively detect the angular and recoil velocity distributions of the $Cl(^2P_{3/2})$ and $Cl(^2P_{1/2})$ atoms to further refine the distribution of internal energy partitioned to the momentum-matched CH_3SO_2 radicals. The internal energy distribution of the radicals is bimodal, indicating that CH_3SO_2 is formed in both the ground state and low-lying excited electronic states. All electronically excited CH_3SO_2 radicals dissociate, while those formed in the ground electronic state have an internal energy distribution which spans the dissociation barrier to CH_3+SO_2. We detect the recoil velocities of the energetically stable methylsulfonyl radicals with 118 nm photoionization. Comparison of the total recoil translational energy distribution for all radicals to the distribution obtained from the detection of stable radicals yields an onset for dissociation at a translational energy of 70 ± 2 kcal/mol. This onset allows us to derive a $CH_3SO_2 \rightarrow CH_3+SO_2$ barrier height of 14 ± 2 kcal/mol; this determination relies on the S–Cl bond dissociation energy, taken here as the CCSD(T) predicted energy of 65.6 kcal/mol. With 118 nm photoionization, we also detect the velocity distribution of the CH_3 radicals produced in this experiment. Using the velocity distributions of the SO_2 products from the dissociation of CH_3SO_2 to CH_3+SO_2 presented in the following paper, we show that our fastest detected methyl radicals are not from these radical dissociation channels, but rather from a primary $S-CH_3$ bond photofission channel in CH_3SO_2Cl. We also present critical points on the ground state potential energy surface of CH_3SO_2 at the CCSD(T)/aug-cc-pV(Q+d)Z//CCSD(T)/6-311++G(2*df*,*p*) level. We include harmonic zero-point vibrational corrections as well as core-valence and scalar-relativistic corrections. The CCSD(T) predicted barrier of 14.6 kcal/mol for $CH_3SO_2 \rightarrow CH_3+SO_2$ agrees well with our experimental measurement. These results allow us to predict the unimolecular dissociation kinetics of CH_3SO_2 radicals and critique the analysis of prior time-resolved photoionization studies on this system. © *2009 American Institute of Physics*. [DOI: 10.1063/1.3159556]

I. INTRODUCTION

CH_3SO_2 adduct formation and destruction is key to the temperature dependence in models of the atmospheric oxidation of dimethylsulfide,[1] the major natural source of sulfur in the troposphere. To investigate the unimolecular dissociation of CH_3SO_2, we first present high-level CCSD(T) calculations of critical points on the ground state potential energy surface of CH_3SO_2. To benchmark the CCSD(T) calculations, we experimentally determine the unimolecular dissociation barrier for $CH_3SO_2 \rightarrow CH_3+SO_2$ using a method[2,3] particularly well suited to radical systems. We also characterize CH_3SO_2Cl as a photolytic precursor to the CH_3SO_2 radical. The measured velocity and angular distributions evidence three primary photodissociation channels. These experiments reveal the source of the dynamics observed in prior time-resolved photoionization studies of the CH_3SO_2 radical and provide the electronic structure results necessary to theoretically predict the thermal dissociation kinetics of the radical.

One important goal of this study is to further develop our predictive ability for sulfur-containing radicals using CH_3SO_2 as a benchmark. Based on their theoretical study of the CH_3S+O_2 reaction system, Zhu and Bozzelli[4] recommended that enthalpy values from the G3MP2 and CBS-QB3 composite methods be used for carbon-sulfur-oxygen systems, when feasible. They further noted that their CCSD(T)/6-311G(*d*,*p*)//MP2/6-31G(*d*,*p*) calculations did not give accurate results. This motivated the portion of the work herein where we investigate the basis set dependence of the CCSD(T) results on this system, as one expects that the CCSD(T) method would give more reliable predictions than the composite methods. The importance of including inner-core polarization functions in the basis sets for sulfur-

a)Authors to whom correspondence should be addressed. Electronic addresses: L-Butler@uchicago.edu and kaichung@cityu.edu.hk.

TABLE I. Unimolecular dissociation rates measured for CH_3SO_2.

	$k(T,P)$ (s^{-1})	T, P
Le Bras, 2003 (Ref. 12)	≤ 1 [a]	300 K, 100–600 Torr
Le Bras, 2000 (Ref. 13)	≤ 100 [a]	300 K/20–600 Torr
	≤ 50 [a]	300 K/1 Torr
Le Bras, 1996 (Ref. 14)	510 ± 150	298 K/1 Torr
Owrutsky, 2001 (Ref. 16)	3×10^{12}	Nonthermal, $P=0$ (photolysis with undetermined E_{int})

[a]These rely on the assumption that the rate of $CH_3SO+NO_2 \rightarrow CH_3+SO_2+NO$ is 1.5×10^{-11} cm^3 $molecule^{-1}$ s^{-1}. This reaction seems to be an attempt to distinguish between the thermal unimolecular decomposition of CH_3SO_2 formed initially in the reaction of CH_3SO+NO_2 and the direct formation of CH_3+SO_2+NO from the bimolecular reaction of CH_3SO+NO_2.

containing compounds was first noted in 1998. Martin *et al.* found that the inclusion of inner-core polarization functions made tremendous improvements to the theoretical predictions of the binding energies and atomization energies for SO_x $(x=1-3)$ molecules.[5,6] Later, Dunning *et al.*[7] modified the standard correlation-consistent polarization basis sets by augmenting tight *d*-functions to improve the basis set convergence for electron correlation on sulfur and other third-row elements (often referred to as "second-row elements" in electronic structure papers[5]). With the tight *d*-augmented correlation-consistent basis sets, Wilson, Dunning and co-workers[8–11] investigated the effects of the basis sets on the energetic and structural predictions for the SO_2, SO_3, and HOS/HSO molecules using CCSD(T) and density functional theory methods. Their studies show that the revised correlation-consistent basis sets improve basis set convergence and reduce the deviations of the theoretical predictions from the experimental values. In this study, we employ the correlation-consistent basis sets augmented with tight *d*-polarization functions at the CCSD(T) level to explore the potential energy surface for the dissociation and isomerization of the CH_3SO_2 radical. We also include the core-valence correlation and relativistic corrections in our calculations. Although we used some of the smaller basis sets available in the correlation-consistent basis set series, the predicted forward barrier height for $CH_3SO_2 \rightarrow CH_3+SO_2$ converged to 0.9 kcal/mol (see results below). Thus, our results also show that the tight *d*-augmented correlation-consistent basis sets are good for predicting barrier energies at the transition state (TS) of chemical reactions involving polyatomic radicals. We hope our study will guide future work on the size of the basis and nature of the corrections needed to obtain accurate electronic structure predictions on radicals containing third-row atoms.

Table I summarizes the published work on the unimolecular dissociation rate of CH_3SO_2. Le Bras and co-workers[12–14] indirectly determined the dissociation rate of CH_3SO_2 with kinetic modeling of gas mixtures in their pulsed photolysis/laser-induced fluorescence and discharge flow mass spectrometry/laser-induced fluorescence experiments. The difficulty of obtaining accurate dissociation rates for the CH_3SO_2 radical from the modeling in these bulk experiments is evident; the dissociation rates reported by Le Bras and co-workers are upper bounds only, with rate constants ranging from ≤ 50 to 510 ± 150 s^{-1} at 300 K and 1 Torr. They compare their results to predictions of unimolecular dissociation rates based on the TS calculated by Frank and Turecek.[15] The comparison is only qualitative because they assume that the internal energy of the CH_3SO_2 radicals is determined by the calculated exoergicity of the bimolecular reaction that produces the radicals. (CH_3SO_2 radicals are formed from the bimolecular reaction of CH_3SO+NO_2, so the internal energy content is taken from an assumed energy partitioning of the calculated exoergicity of this bimolecular reaction to the CH_3SO_2+NO products summed with $\frac{1}{2}$ RT thermal energy in each vibrational mode of CH_3SO_2.) Additionally, the rates of Le Bras and co-workers are not in the high-pressure limit, so they estimate the fall-off due to collisional energy transfer. At $k_{uni} \leq 100$ s^{-1}, the fits to the measured CH_3O profiles are insensitive to the unimolecular dissociation rate.

Using femtosecond mass-resolved photoionization spectroscopy, Owrutsky *et al.*[16] measured a dissociation lifetime of 0.34 ps for CH_3SO_2 radicals produced from the 196 nm photodissociation of CH_3SO_2Cl. They observed that fewer than 2% of the nascent CH_3SO_2 radicals remain after 2 ps. They statistically modeled their results with RRKM theory using the $CH_3SO_2 \rightarrow CH_3+SO_2$ TS published by Frank and Turecek.[15] Since they could not directly measure the internal energy distribution of the nascent radicals, they chose an internal energy distribution for their statistical model which agreed with their measured experimental lifetime of 0.34 ps. This internal energy distribution peaked at 24 kcal/mol and extended below the dissociation barrier, predicting that 13% of the nascent radicals would remain after 2 ps. Thus their assumed internal energy distribution was unable to match both the measured experimental lifetime of the radicals and the percent of undissociated radicals at 2 ps. This motivated us to directly determine the internal energy distribution of nascent CH_3SO_2 radicals produced from the photodissociation of CH_3SO_2Cl at 193 nm in these experiments.

The experiments below, in conjunction with those presented in the following paper,[17] characterize the internal energy distribution of the CH_3SO_2 radicals produced from the photodissociation of CH_3SO_2Cl. They further determine the internal energy onset for dissociation of the radicals to CH_3+SO_2, and thus offer a definitive benchmark for electronic structure calculations on radicals containing third-row atoms. Surprisingly, we learn that the prior promising rate measurements by Owrutsky *et al.* were unknowingly detecting the dissociation rate of electronically excited radicals. In the discussion, we assess both the basis set convergence of the high-level CCSD(T) predictions for the TS for this reaction, and we suggest an experimental methodology for determining the microcanonical unimolecular rates for this reaction without interference from the dissociation of the electronically excited radicals.

II. EXPERIMENT

This experimental setup has been previously described in detail,[18–21] so only a brief description and modifications are provided here. A 10% molecular beam was created by

bubbling helium gas through a liquid sample of methylsulfonyl chloride (Fluka, >99%) at room temperature. At a total stagnation pressure of 500 Torr, the molecular beam was supersonically expanded through a room temperature General Valve Iota One pulsed valve with an orifice diameter of 0.8 mm. After passing through a skimmer the molecules were photodissociated with a 193.3 nm beam generated from a GAM (EX10F/300) ArF laser. The 8×4 mm^2 beam was focused with a 250 mm lens, with the focal point about 1 cm after the intersection with the molecular beam. Typical pulse energies were less than 1 mJ/pulse, eliminating multiphoton effects. When studying the angular distribution of the photodissociation of CH_3SO_2Cl, the 193 nm beam first passed through a single crystal quartz birefringent Pellin–Broca to separate the unpolarized light into two linearly polarized beams. The beam with vertical polarization was focused into the main chamber.

Using 2+1 resonance-enhanced multiphoton ionization (REMPI), the Cl($^2P_{3/2}$) and Cl($^2P_{1/2}$) photofragments were state-selectively ionized using 235.33 nm ($4p\ ^2D_{3/2} \leftarrow 3p\ ^2P_{3/2}$) and 235.20 nm ($4p\ ^2P_{1/2} \leftarrow 3p\ ^2P_{1/2}$) wavelengths, respectively.[22] The accumulated signals were obtained by scanning the Doppler profiles ± 0.008 nm from line center. The 235 nm laser beam was generated by tripling the output of a dye laser (Lambda Physik, FL 3002, LDS 698 dye) which was pumped by the second harmonic of a pulsed injection-seeded Nd:YAG (yttrium aluminum garnet) laser (Continuum Powerlite Precision 9020). To triple the dye laser output, the ~706 nm beam was frequency doubled in a potassium dihydrogen phosphate crystal and the resulting 353 nm light was mixed with the 706 nm fundamental in a beta-barium borate crystal to produce vertically polarized 235 nm photons.

The methylsulfonyl and CH_3 radical products were ionized with 118 nm light generated by tripling the 355 nm output beam from a second pulsed Nd:YAG laser (Continuum Surelite I-20). The 355 nm beam was first expanded with a beam expander (focal length=−150 mm and focal length=300 mm at 588 nm). A lens (focal length of ~25.4 cm) then tightly focused the 355 nm beam into a ~21 cm low pressure gas cell filled with ~25 Torr of high purity Xe. The gas cell was mounted onto the main vacuum chamber with a MgF_2 lens (focal length=120.3 mm at 193 nm) serving as the barrier between the cell and the chamber.

The electrostatic lens optics with a repeller:extractor voltage ratio of 1.414:1 accelerated the spherically expanding ions down a ~577 mm grounded time-of-flight tube toward the detector (Burle 3040FM). The detector consisted of a position-sensitive Chevron microchannel plate (MCP) assembly coupled to a P20 phosphor screen. The voltage of the front plate of the MCP was pulsed to −750 V for 80 ns to mass selectively detect ions based on their arrival time. The timing of this voltage drop was optimized for signal intensity. The phosphor screen was maintained at 3.3 kV above the potential of the rear MCP plate. A cooled charge-coupled device camera (La Vision Imager 3) with a standard 35 mm lens was used to grab images of the ions, which were processed using the ion-counting method.[23] The raw images were symmetrized about the vertical and horizontal axes in the data analysis.

The 20 Hz timing for the opening of the pulsed valve, firing the lasers, pulsing the MCP detector voltage, and capturing the images was controlled by a digital delay generator (Stanford Research DG 535). The photolysis laser was fired ~30 ns prior to the ionization laser.

III. THEORETICAL CALCULATIONS

The important minima and TSs on the potential energy surface for the dissociation and isomerization processes of CH_3SO_2 and the S–Cl bond energy (D_0) in CH_3SO_2Cl were evaluated at the coupled-cluster level with single and double excitations plus a quasiperturbative triple excitation[24] [CCSD(T)] together with Dunning's correlation-consistent basis sets.[7,25] Specifically, the geometries of CH_3SO_2Cl, CH_3SO_2, *cis*-/*trans*-CH_3OSO, CH_3, SO_2, CH_3O, CH_2O, SO, HOS and the TS structures were optimized at the CCSD(T)/6-311++G(2*df*,*p*) level. Based on the optimized structures, single-point frozen-core energy calculations were carried out at the CCSD(T)/aug-cc-pV(Q+d)Z level of theory.

Corrections for the zero-point vibrational energy (ZPVE) and core-valence electron correlation effects were included. The harmonic ZPVE was calculated at the CCSD(T)/6-311++G(2*df*,*p*) level. The core-valence electron correlation (1*s* electrons on C and O, 2*s*/2*p* electrons on S and Cl) was obtained at the CCSD(T) level using a cc-pwCVTZ basis set.[26] A correction for relativistic effects was obtained using the spin-free, one-electron Douglas–Kroll–Hess Hamiltonian[27] at the CCSD(T)/aug-cc-pVTZ-DK level. All the CCSD(T) single-point energies, vibrational frequencies, and correlation contributions were calculated with the MOLPRO 2006.1 program.[28] The atomic spin-orbit correction for Cl was taken from C. Moore's compilation.[29] All of the relevant structures, harmonic vibrational frequencies, rotational constants, energies, and energy corrections calculated for these CCSD(T) results are given in the supplementary EPAPS document.[30]

CIS(D) calculations of the excited CH_3SO_2Cl electronic states were calculated with a 6-311++G(2*df*,*p*) basis using the GAUSSIAN 03 program, revision E.01.[31]

IV. RESULTS

A. CCSD(T) predictions for the dissociation and isomerization processes of CH_3SO_2

Figure 1 depicts the minima and TSs on the potential energy surface for the dissociation and isomerization processes of the CH_3SO_2 radical. (The energies shown in the figure include a harmonic ZPVE correction). There are three stable minimum structures on the potential energy surface (with the exception of those due to the internal methyl rotor): ground state $CH_3SO_2(^2A')$, *cis*-CH_3OSO, and *trans*-CH_3OSO. There is also a shallow local minimum along the reaction coordinate for CH_3SO_2 to dissociate to $CH_3 + SO_2$. The CH_3SO_2 radical may isomerize to *cis*-CH_3OSO via a TS with a barrier of 47.6 kcal/mol (relative to

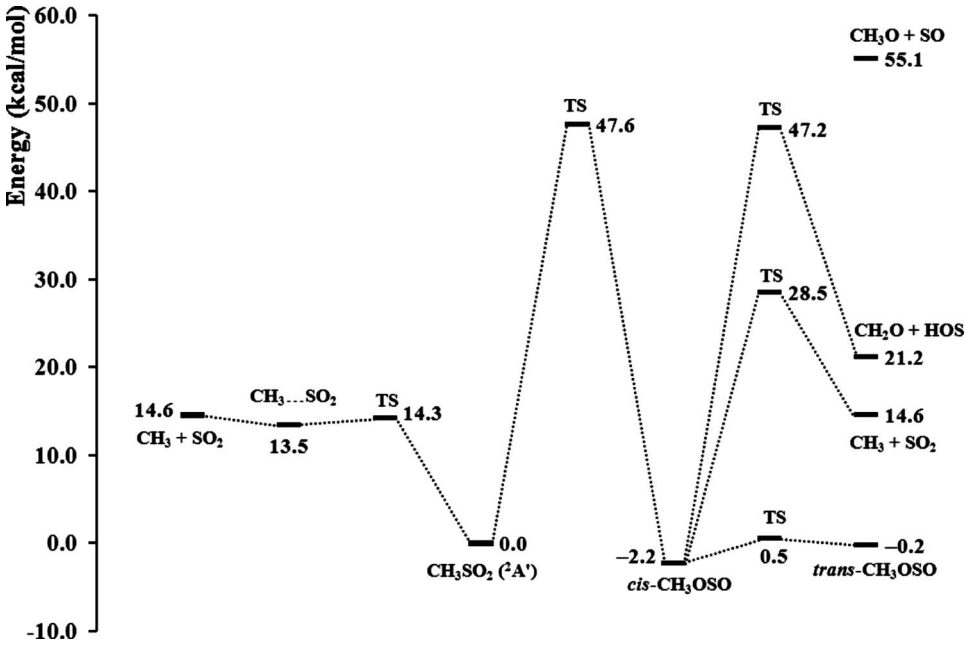

FIG. 1. The mimina, TSs, and product channels on the potential energy surface for CH_3SO_2 calculated using the CCSD(T) method.

CH_3SO_2). The *cis*-CH_3OSO radical is more stable than the CH_3SO_2 radical by 2.2 kcal/mol. The isomerization barrier between *cis*-CH_3OSO and *trans*-CH_3OSO is quite small (2.7 kcal/mol relative to *cis*-CH_3OSO). Thus, the interconversion between *cis*-CH_3OSO and *trans*-CH_3OSO conformers is energetically very feasible. The CH_3SO_2 radical goes through a TS (with a barrier height of 14.3 kcal/mol relative to CH_3SO_2) to form a weak intermediate complex, $CH_3\cdots SO_2$. This complex then dissociates to methyl radical and sulfur dioxide. The *cis*-CH_3OSO radicals dissociate to CH_3+SO_2 through a TS with a barrier height of 30.7 kcal/mol (relative to *cis*-CH_3OSO). Thus, the CH_3SO_2 radical has two dissociation pathways to yield the CH_3+SO_2 products: one is a direct path through the $CH_3\cdots SO_2$ intermediate complex, and the other involves isomerization to *cis*-CH_3OSO followed by the dissociation of *cis*-CH_3OSO. The former pathway (having a barrier height of 14.3 kcal/mol relative to CH_3SO_2 to reach the $CH_3\cdots SO_2$ intermediate complex and no barrier beyond the 14.6 kcal/mol endoergicity to dissociate fully) is energetically more favorable than the latter, which requires traversing a 47.6 kcal/mol barrier to isomerize to CH_3OSO. The CH_3OSO radical then dissociates to CH_3+SO_2 via a tight TS (the barrier to form CH_2O+HOS is nearly 20 kcal/mol higher).

Table II gives details of the key computational elements needed to accurately predict the energetics of the dissociation and isomerization channels of the CH_3SO_2 radical. The total energy is the sum of the electronic energy at the CCSD(T)/aug-cc-pV(Q+d) level, the ZPVE correction obtained at the CCSD(T)/6-311++G(2*df*,*p*) level, and the corrections for core-valence electron correlations and relativistic effects. The energies at the CCSD(T)/6-311++G(2*df*,*p*) and CCSD(T)/aug-cc-pV(T+d)Z levels are also included for comparison. The energetics at the CCSD(T)/6-311++G(2*df*,*p*) of most stationary points are roughly similar to these reported by Zhu and Bozzelli[4] at the G3(MP2) level. However, when a correlation-consistent basis set, such as aug-cc-pV(T+d)Z, is used, the relative energies at the aug-cc-pV(T+d)Z level for all minima, TS structures, and asymptotes increase by 0.7–5.3 kcal/mol relative to those at the CCSD(T)/6-311++G(2*df*,*p*) level. The most significant relative energy changes are for the CH_3O+SO and CH_2O+HOS asymptotes, whose energies change by more than 5 kcal/mol. Further enlargement of the basis sets from aug-cc-pV(T+d)Z to aug-cc-pV(Q+d)Z increases the relative energies of all stationary points by 1–2 kcal/mol, except for the CH_3O+SO and CH_2O+HOS asymptotes where the relative energy with the aug-cc-pV(Q+d)Z basis set [compared with those using an aug-cc-pV(T+d)Z basis set] increases by ~3.5 kcal/mol. Martin *et al.*[5,6] suggested that the inner-core polarization functions are important for an accurate description of the valence electron correlation in the SO_x species ($x=1-3$). Thus, the relative energetics of the CH_3O+SO and CH_2O+HOS asymptotes change significantly when the size of the basis is increased from 6-311++G(2*df*,*p*) to aug-cc-pV(T+d)Z. There are no inner-core polarization functions in the former basis while there is an "extra" *d*-type inner polarization function (with a high exponent) in the aug-cc-pV(T+d)Z basis set. Lack of high-exponent functions on the sulfur atom (and other third-row elements) in the standard correlation-consistent polarization valence basis set also led to the development of the aug-cc-pV(X+d)Z basis sets by Dunning *et al.*[7] in 2001. The relative energy changes from the aug-cc-pV(T+d)Z to the aug-cc-pV(Q+d)Z basis set are less prominent because the electronic energetics are more closely converged to the basis set limit. Previous experience on the correlation-consistent basis sets indicates that the electronic energies would converge better when even larger aug-cc-pV(5+d)Z basis sets are used. However, such single-point energy calculations at the CCSD(T)/aug-cc-pV(5+d)Z level are computationally demanding, especially for molecules which lack symmetry.

The forward dissociation barrier for $CH_3SO_2\rightarrow CH_3+SO_2$ is 14.3 kcal/mol to reach the $CH_3\cdots SO_2$ intermediate complex and an additional 0.3 kcal/mol to reach the product

TABLE II. The individual energetic contributions and total energy of all stationary points on the potential energy surface of Fig. 1. All energies, in kcal/mol, are relative to the zero-point level of CH_3SO_2.

Energetic contribution	*cis*-CH_3OSO	*trans*-CH_3OSO	CH_3O+SO	CH_2O+HOS	CH_3+SO_2
E[CCSD(T)/6-311++G(2df,p)]	−6.3	−3.5	50.5	17.6	17.6
E[CCSD(T)/aug-cc-pV(T+d)Z]	−3.9	−1.3	55.8	22.6	19.5
E[CCSD(T)/aug-cc-pV(Q+d)Z]	−2.5	0.1	59.3	25.0	20.4
ZPVE[a]	0.7	0.1	−3.7	−3.4	−5.4
Core-valence correlation[b]	0.1	0.1	0.2	0.2	0.1
Scalar-relativistic correction[c]	−0.5	−0.5	−0.7	−0.6	−0.5
Total relative energy[d]	−2.2	−0.2	55.1	21.2	14.6

Energetic contribution	CH_3SO_2 _TS_ CH_3+SO_2	CH_3SO_2 _TS_ *cis*-CH_3OSO	*cis*-CH_3OSO _TS_ CH_3+SO_2	*cis*-CH_3OSO _TS_ CH_3+HOS	*cis*-CH_3OCO _TS_ *trans*-CH_3OCO	$CH_3\cdots SO_2$ [e]
E[CCSD(T)/6-311++G(2df,p)]	16.4	47.7	29.4	44.9	−3.3	···
E[CCSD(T)/aug-cc-pV(T+d)Z]	17.3	48.4	30.5	48.5	−0.9	17.3
E[CCSD(T)/aug-cc-pV(Q+d)Z]	18.2	49.8	31.9	51.4	0.5	18.2
ZPVE[a]	−3.6	−1.9	−3.1	−3.7	0.5	−4.3
Core-valence correlation[b]	0.1	0.3	0.2	0.2	0.0	0.1
Scalar-relativistic correction[c]	−0.4	−0.6	−0.5	−0.7	−0.5	−0.5
Total relative energy[d]	14.3	47.6	28.5	47.2	0.5	13.5

[a]ZPVE is obtained at the CCSD(T)/6-311++G(2df,p) level.
[b]The core-valence correlation is obtained at the CCSD(T)/cc-pwCVTZ level.
[c]The relativistic effect is obtained at the CCSD(T)/aug-cc-pVTZ-DK level using the Douglas–Kroll–Hess Hamiltonian.
[d]The total energy is the sum of E[CCSD(T)/aug-cc-pV(Q+d)Z], ZPVE, core-valence, and scalar-relativistic corrections. This sum for the CH_3SO_2 radical is taken to be zero.
[e]The structure of this intermediate is optimized at the CCSD(T)/aug-cc-pV(T+d)Z level, see text for details.

asymptote (relative to the zero-point level of the CH_3SO_2 radical). As mentioned before, the C–S bond fission of the CH_3SO_2 radical *en route* to form CH_3 and SO_2 involves the formation of an intermediate complex, $CH_3\cdots SO_2$. At the CCSD(T)/6-311++G(2df,p) level, the C–S bond lengths are 1.818 in CH_3SO_2 and 2.627 Å in the TS at 14.3 kcal/mol. At longer C–S bond lengths, we could not locate the $CH_3\cdots SO_2$ intermediate at the CCSD(T)/6-311++G(2df,p) level. The reported intermediate structure was found at the CCSD(T)/aug-cc-pV(T+d)Z level. Therefore, the ZPVE, core-valence electronic and relativistic calculations of the $CH_3\cdots SO_2$ intermediate are based on the optimized structure at the CCSD(T)/aug-cc-pV(T+d)Z level. The existence of this intermediate structure is indirectly supported by the fact that the TS structure is lower in energy than the fully dissociated fragments of CH_3+SO_2 at the CCSD(T)/aug-cc-pV(T+d)Z level. At the CCSD(T)/aug-cc-pV(T+d)Z level, the C···S distance in the intermediate is 2.985 Å and the barrier beyond the endoergicity to reach this complex from CH_3SO_2 is 0.8 kcal/mol. Due to the good agreement obtained between our theoretical predictions and the experimental measurement to the dissociation barrier for $CH_3SO_2 \rightarrow CH_3+SO_2$ process (see discussion below), we recommend that the aug-cc-pV(X+d)Z basis set with an additional *d*-type polarization function be used for barrier height predictions for the dissociation of sulfur-containing radicals.

B. Total recoil translational energy distribution from methylsulfonyl chloride photodissociation

The total recoil translational energy distribution for S–Cl bond fission from the 193 nm photodissociation of methylsulfonyl chloride is determined by detecting the recoiling Cl photofragments at a mass to charge ratio of 35. An example of the ion images is shown in Fig. 2. This experiment was conducted in two different ways, first with the photolysis laser unpolarized in the plane perpendicular to the image and then with the photolysis laser vertically polarized. The former method results in larger signal and better signal to noise; it was used to determine the total recoil translational energy distribution for S–Cl bond fission described below. The latter method resulted in poorer signal to noise and difficult background subtraction (described in the attached EPAPS supplement, Fig. S.1—Fig. S.5). Thus the data taken with the polarized 193 nm beam were used only to determine the angular distribution of the recoiling Cl fragments. The Cl images in Fig. 2 were obtained with a vertically polarized photolysis laser.

The three-dimensional scattering distribution is reconstructed from each image with an inverse Abel transformation.[32] The speed distributions $P_{Cl}(v)$ of the Cl fragments are extracted by integrating the three-dimensional velocity distributions over all solid angles at each speed and accounting for the appropriate Jacobian. Using momentum conservation, the center-of-mass recoil translational energy distributions $P(E_T)$ for $CH_3SO_2Cl \rightarrow CH_3SO_2+Cl$ are derived from the Cl speed distributions. We use the Cl images taken with an unpolarized photolysis laser (shown in Fig. S.1 of the EPAPS supplement) to obtain the $P(E_T)$ shown in Fig. 3. Also shown is the total S–Cl bond fission $P(E_T)$, which is the sum of the kinetic energy distributions for the $CH_3SO_2+Cl(^2P_{3/2})$ and the $CH_3SO_2+Cl(^2P_{1/2})$ channels, weighted by the $Cl(^2P_{3/2}):Cl(^2P_{1/2})$ spin-orbit branching ratio of $2.3\pm0.3:1$. The branching ratio was found by integrating the

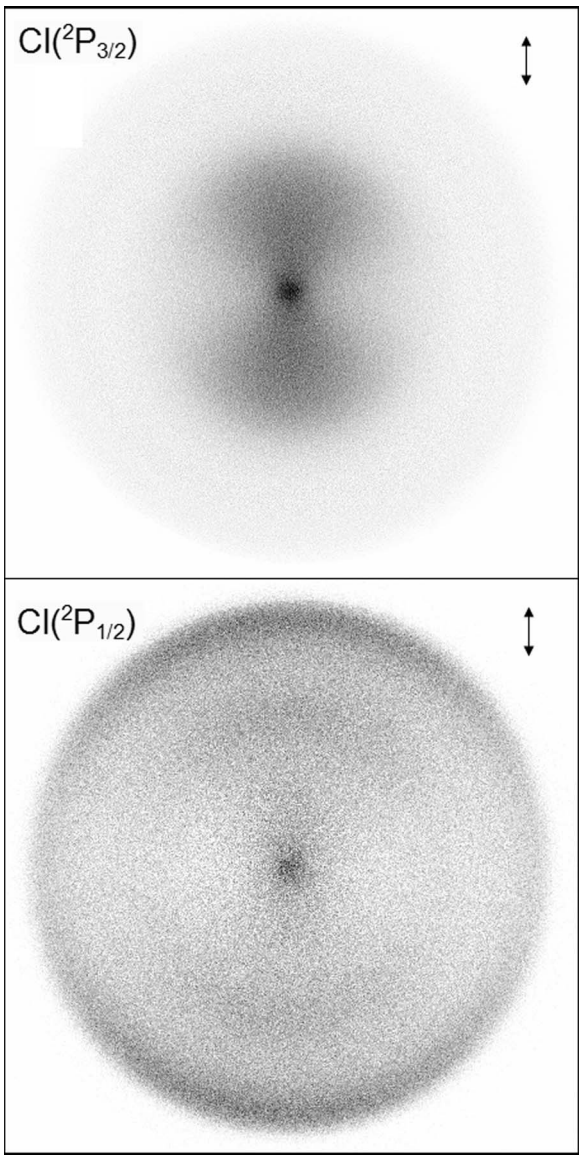

FIG. 2. Background subtracted images of 193 nm photodissociation of CH_3SO_2Cl followed by photoionization of $Cl(^2P_{3/2})$ (top) and $Cl(^2P_{1/2})$ (bottom). For these data, the 193 nm photolysis laser was vertically polarized, as shown with the arrows. The repeller voltage was 3932 V and the extractor voltage was 2800 V. The images depicted are 901×901 pixels. Images from 193 nm only and 235 nm only were subtracted from the raw data to obtain this image.

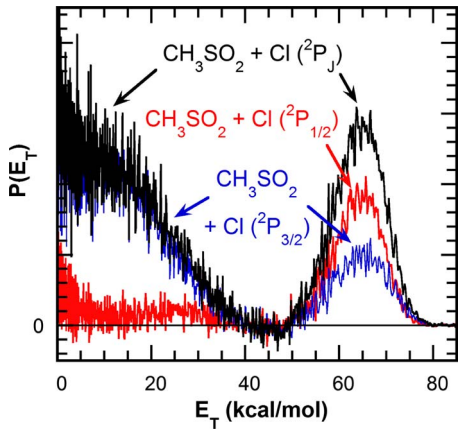

FIG. 3. The total recoil kinetic energy distributions obtained from the detection of $Cl(^2P_{3/2})$ (blue/thin black line) and $Cl(^2P_{1/2})$ (red/grey line) using unpolarized 193 nm photodissociation light. The normalized total CH_3SO_2 +Cl $(^2P_{1/2,3/2})$ center-of-mass recoil translational energy distribution is shown in black solid line.

total ion signal from each Cl spin-orbit state in images accumulated over the entire Doppler profile and weighting the result by the REMPI line strength.[33] The error bars show the 95% confidence interval from six independent trials.

In Sec. IV E, we cite evidence of another minor primary photolysis channel, $CH_3SO_2Cl \rightarrow CH_3 + SO_2Cl$. SO_2Cl radicals formed from the $S-CH_3$ bond fission in the precursor then undergo secondary dissociation to SO_2+Cl. Cl atoms formed via this dissociation pathway are characterized by slow recoil velocities. They contribute to the signal near the center of the Cl images which are used to derive the $P(E_T)$ for S–Cl bond fission shown in Fig. 3, so this $P(E_T)$ is overvalued at $E_T < 5$ kcal/mol.

The $P(E_T)$ for the dissociation events forming $Cl(^2P_{3/2})$ is bimodal peaking at 10 and 65 kcal/mol; it is reproducible within ± 1 kcal/mol. However, as described below it may be influenced by systematic errors. The $P(E_T)$ for the dissociation events forming $Cl(^2P_{1/2})$ is dominated by a sharp high-kinetic-energy distribution peaked at 65 kcal/mol. The tiny signal near 25 kcal/mol in the $Cl(^2P_{1/2})$ contribution to Fig. 3 results from multiphoton absorption of 193 nm followed by 235 nm ionization. Although multiphoton contributions may be eliminated at low laser powers, the signal to noise of the remaining signal is poor. Thus, the variation in this low kinetic energy portion of the $Cl(^2P_{1/2})$ signal affects the spin-orbit branching ratio and ultimately the shape of the fast component in the normalized $P(E_T)$ when the two high kinetic energy Cl distributions are summed. The $P(E_T)$ reported in Fig. 3 and the spin-orbit branching ratio were obtained from the same trials to minimize the uncertainty in the $P(E_T)$.

The bimodal $P(E_T)$ indicates that the photodissociation of CH_3SO_2Cl at 193 nm forms CH_3SO_2 radicals in both the ground and excited electronic states. In the following paper we confirm this assignment with excited state electronic structure calculations and measurements of the dissociation dynamics of the ground and excited state radicals. Radicals formed in the high recoil kinetic energy region are formed in the $\tilde{X}\,^2A'$ ground electronic state. Radicals formed in the low kinetic energy region are in excited electronic states; the onset of this signal roughly corresponds to the 34.8 kcal/mol calculated adiabatic excitation energy of the $1\,^2A''$ excited state.

As shown in Fig. S.6, our total recoil translational energy distribution is in qualitative agreement with that obtained from the scattering apparatus, which is presented in the following paper. While both distributions are bimodal and indicate the formation of CH_3SO_2 radicals in both the ground and low-lying excited electronic states, some quantitative differences are apparent. Integrating the high and low kinetic energy portions of the S–Cl fission $P(E_T)$ determined in the scattering experiment gives 43% as Cl + excited state CH_3SO_2 and 57% as Cl + ground state CH_3SO_2. The imaging results shown in Fig. 3 and in Fig. S.6 show a larger

branching to the excited state radical channel, with 62% as Cl + excited state CH_3SO_2 (E_T=0–45 kcal/mol) and 38% as Cl + ground state CH_3SO_2 (E_T=45–80 kcal/mol). However, some of the Cl atoms present in the imaging $P(E_T)$ at $E_T < 5$ kcal/mol may be due to Cl atoms from the dissociative SO_2Cl formed in the minor CH_3+SO_2Cl channel; 14% of the imaging $P(E_T)$ has $E_T < 5$ kcal/mol. This signal overlaps the clusters in the scattering experiments so it was subtracted from the scattering $P(E_T)$ but not the imaging $P(E_T)$. This additional channel does not completely compensate for the difference in observed branching between the excited and ground state channels. If all the observed imaging signal below 5 kcal/mol originated from the primary S–Cl bond fission channel, the remaining imaging data would evidence 56% as Cl + excited state CH_3SO_2 and 44% of Cl + ground state CH_3SO_2. More surprisingly, the high kinetic energy portion of the imaging $P(E_T)$ in Fig. 3 is approximately 8 kcal/mol narrower than the scattering $P(E_T)$ when measured at the full width half maximum. The next paragraph summarizes our attempts at resolving this discrepancy. We conclude that the $P(E_T)$ obtained from the scattering data is less subject to systematic error, so we use that $P(E_T)$ rather than the one in Fig. 3 for the analysis in Secs. IV C and IV D.

We detected the recoiling Cl atoms under many different photodissociation and ionization conditions in an attempt to resolve the differences between our $P(E_T)$ and that obtained from the scattering experiment. Limited 193 and 235 nm power dependence studies did not reveal any multiphoton contribution in the background subtracted signal [except for the previously noted small peak in the $Cl(^2P_{1/2})$ signal at 25 kcal/mol]. We investigated the presence of clusters by seeding the CH_3SO_2Cl precursor in both Ar and He carrier gases. We saw no difference between the $P(E_T)$'s from these trials. Because the recoil velocities of the Cl atoms are quite high in this experiment, we also carefully considered the possibility that using a single ion flight time when converting from the imaging pixel distribution to a speed distribution might artificially narrow the $P(v)$ and resulting $P(E_T)$. However, detailed ion trajectory simulations show that the Cl $P(E_T)$ calculated from the data using this assumption is narrowed by less than 1 kcal/mol. Finally, we investigated the possibility that the fastest Cl atoms were escaping detection by flying out of the region before they were ionized by more tightly focusing the 193 nm photodissociation laser, but this resulted in overwhelming multiphoton signal. Moving the intersection region further from the focus of 235 nm photoionization laser decreased the REMPI signal below that needed for good signal to noise. Unable to eliminate this as a possible source of error, we tentatively ascribe the mismatch between the fast edge of the imaging and scattering S–Cl bond fission $P(E_T)$ to the flyout of the Cl atoms from the ionization volume.

C. Total recoil kinetic energy distribution for photodissociation events that result in stable CH_3SO_2 radicals

Ionization and detection of the methylsulfonyl radical cofragments provide a measurement of the total recoil kinetic energy distribution for photodissociation events that result in stable radicals. We ionize the CH_3SO_2 photofragments (ionization potential of 9.72 eV, calculated using the G3X method) with 118 nm light (10.5 eV); the resulting raw image is shown in Fig. 4. Photoionization of CH_3SO_2 radicals at 118 nm results in signal at the parent's mass to charge ratio of 79, $CH_3SO_2^+$. Interestingly, as described in the following paper, electron bombardment ionization of the stable CH_3SO_2 radicals (which are identified by their measured velocity distribution) results in cracking of the $CH_3SO_2^+$ ions to CH_3^+ daughter ions but not signal at the parent mass.

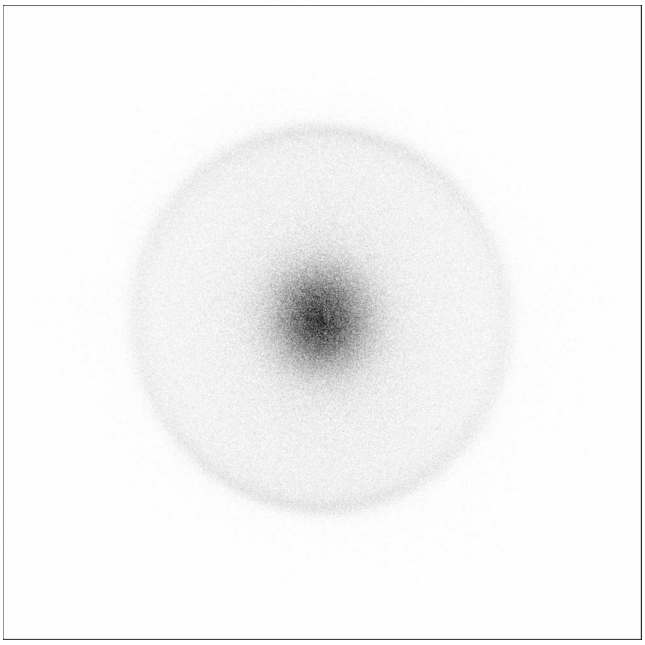

FIG. 4. Raw image containing the CH_3SO_2 fragments resulting from 193 nm photolysis and 118 nm photoionization to $CH_3SO_2^+$. The photolysis laser was polarized in the vertical plane perpendicular to the image. The repeller voltage was 4000 V and the extractor voltage was 2848 V. The image is 901×901 pixels.

The signal appearing at the center of the image in Fig. 4 at low translational energy is background signal due to photodissociation and photoionization with 118 nm only and 193 nm only. This multiphoton signal is strongly dependent on laser power and the 118 nm background is especially difficult to subtract since the Xe gas requires refilling hourly. Fortunately, this background has little contribution in the high recoil kinetic energy region. Thus, we scale the speed distribution from 118 nm dissociation and ionization so that the baseline signal oscillates around zero from v=0 to 1100 m/s (see the EPAPS supplement, Fig. S.7 for further details). The high-translational energy component is from the photodissociation of methylsulfonyl chloride at 193 nm and ionization of stable CH_3SO_2 radicals at 118 nm.

To derive the translational energy distribution for the detected methylsulfonyl radicals, a forward-convolution method[3] was used to account for the fact that stable radicals are momentum matched to both ^{35}Cl and ^{37}Cl atoms. Although the speed distribution of the radicals is shifted to faster speeds if the radical is momentum matched to the heavier isotope, the $P(E_T)$ for these two processes should be nearly identical. Thus, we iteratively adjust a total recoil ki-

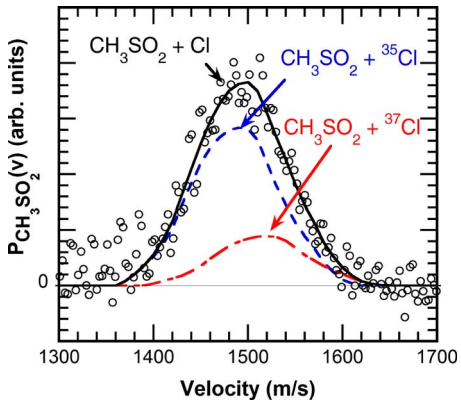

FIG. 5. Speed distribution obtained from the image of stable CH_3SO_2 radicals in Fig. 4 after background subtraction. The experimental data are shown as open circles, and the forward-convolution fit (solid line) is calculated from the total recoil translational energy distribution shown in Fig. 6 by assuming that 75.78% of the radicals recoil from ^{35}Cl (dashed line) and 24.22% recoil from ^{37}Cl (dot-dashed line), in accordance with the isotopic ratio.

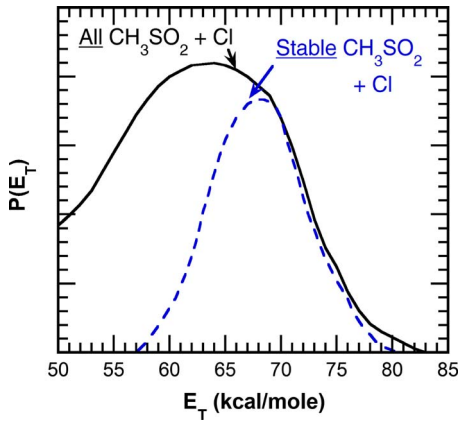

FIG. 7. Total recoil kinetic energy distribution for all photodissociation events with $E_T > 50$ kcal/mol obtained in the scattering studies in the following paper (solid line), shifted to slower kinetic energies by 1 kcal/mol, and the $P(E_T)$ for the production of stable radicals, also shown in dashed line in Fig. 6, obtained from the forward convolution to the image in Fig. 5.

netic energy distribution for stable methylsulfonyl radicals $P(E_T)$ until a good fit to the measured methylsulfonyl radical $P_{CH_3SO_2}(v)$ is achieved. The resulting fitted $P_{CH_3SO_2}(v)$, shown with the experimental data in Fig. 5, is a sum of the speed distributions of the radicals recoiling from each Cl isotope. The $P(E_T)$ used to obtain this forward-convolution fit is shown in dashed line in Fig. 6. To test the reproducibility of the stable CH_3SO_2 $P(E_T)$ distribution, another complete set of data was analyzed; the results and a comparison of the $P(E_T)$s are presented in the supplemental EPAPS document, Figs. S.8–S.10. The two recoil kinetic energy distributions agree quite well on the fast side and have slight variation on the slow edge of the peak.

Figure 6 directly compares the total recoil kinetic energy distribution derived from the Cl images, representing all S–Cl bond fission events, with the recoil kinetic energy distribution for the photodissociation events producing stable

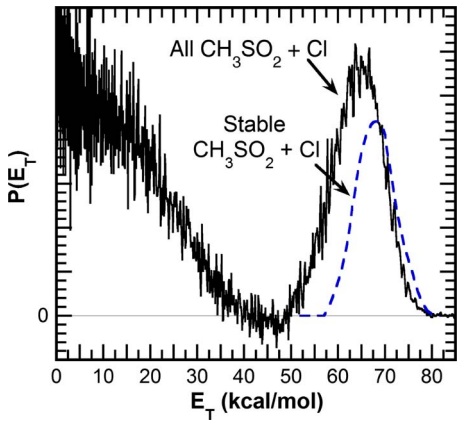

FIG. 6. Center-of-mass translational energy distributions for S–Cl bond fission in methylsulfonyl chloride from photodissociation at 193 nm. The total recoil kinetic energy distribution in black solid line represents all photodissociation events, including both the production of stable and unstable radicals; it is derived from the Cl data. The portion of this distribution that corresponds to the production of energetically stable CH_3SO_2 radicals is shown as the dashed line; it was obtained from the forward-convolution fit to the measured speed distribution of the detected CH_3SO_2 radicals.

methylsulfonyl radicals. As the highest recoil kinetic energy photodissociation events produce radicals with very little internal energy, these $P(E_T)$ should be identical at high-translational energies. We tentatively attribute the mismatch shown in Fig. 6 between the fast edge of the $P(E_T)$ to flyout of the high recoil kinetic energy Cl atoms from the ionization volume. It may also be influenced by the differing ionization volumes in the two measurements, but note that because the 193 nm photodissociation laser is focused tighter than the 118 nm photoionization laser, the ionization volume is determined by the 193 nm beam size. Because the $P(E_T)$ for S–Cl bond fission derived in the scattering experiments are not subject to this difficulty we use that $P(E_T)$ in our analysis below.

Figure 7 compares the total recoil kinetic energy distribution obtained from the scattering apparatus to our $P(E_T)$ for the production of stable radicals to obtain a kinetic energy threshold for the dissociation of CH_3SO_2 radicals. Because the scattering experiment was taken with the precursor heated to 100 °C, we have shifted that reported $P(E_T)$ to lower kinetic energies by 1 kcal/mol in Fig. 7 to account for the difference in vibrational energy in the photolytic precursor between the experiments. The $P(E_T)$s nearly match at high recoil kinetic energy. The forward-convolution fit to the scattering data is not sensitive to the small difference in the $P(E_T)$s on the fast edge. Figure 7 shows that at recoil kinetic energies near 70 kcal/mol, the resulting CH_3SO_2 radicals are left with high enough internal energies to dissociate to $CH_3 + SO_2$. To more precisely determine a dissociation barrier from these data, Fig. 8 shows the percent of dissociated radicals as a function of translational energy. A linear fit to the data between 67.5 and 70 kcal/mol gives a kinetic energy threshold of 70 ± 2 kcal/mol. We only use the onset region for the linear fit because CH_3SO_2 radicals that dissociate within 2.5 kcal/mol of the kinetic energy threshold are formed in conjunction with $Cl(^2P_{3/2})$. As shown in Fig. 3, these photodissociation events are the minor component in this region. Radicals formed in conjunction with $Cl(^2P_{1/2})$ have a kinetic energy threshold of 67.5 kcal/mol, and at this energy, the percent of radicals that dissociate begins to rap-

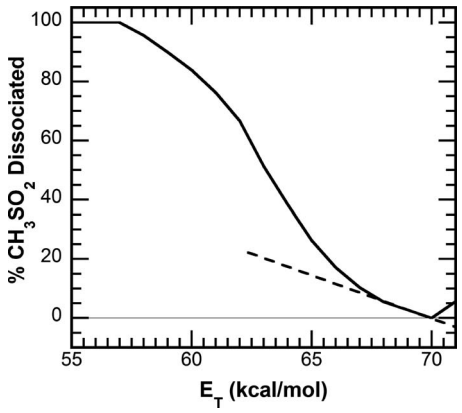

FIG. 8. Percent of dissociated radicals as a function of CH_3SO_2+Cl total recoil kinetic energy (solid line). The *x*-intercept of the linear fit (dashed line) of the data between 67.5 and 70 kcal/mol was used to determine 70 ± 2 kcal/mol as the threshold E_T for methylsulfonyl radical dissociation.

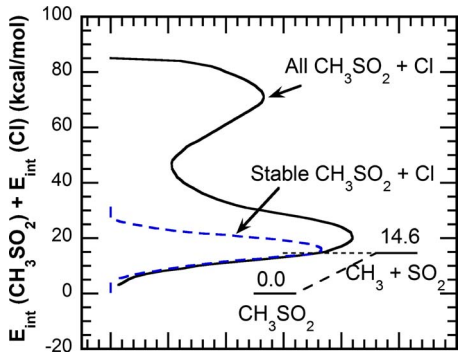

FIG. 9. The measured internal energy distribution (solid line) of all the nascent radicals+Cl atoms is superimposed on the barrier height calculated at the CCSD(T)/aug-cc-pV(Q+d)Z//CCSD(T)/6-311++G(2*df*,*p*) level. The internal energy distribution corresponding to stable radicals+Cl is also shown (dashed line).

idly increase. The survival of radicals with recoil kinetic energy further below this threshold suggests that significant energy is partitioned into rotational energy for some of the CH_3SO_2 radicals. If CH_3SO_2Cl dissociates impulsively from a geometry like its ground state equilibrium geometry, we expect an impact parameter of 0.12 Å. In this case when 65 kcal/mol is partitioned to recoil translational energy, conservation of angular momentum predicts that only 0.4 kcal/mol is partitioned to rotational energy. The observation of higher rotational energies suggests that the photodissociation dynamics on the excited states of CH_3SO_2Cl imparts relative kinetic energy between the fragments at geometries different from the equilibrium geometry of the ground electronic state.

D. Internal energy distribution and barrier height determination

Using energy conservation, the internal energy, rotational plus vibrational, of the nascent radicals $E_{\text{int}}(CH_3SO_2)$ is calculated from

$$E_{\text{int}}(CH_3SO_2) = E_{h\nu} + E_{\text{int}}(CH_3SO_2Cl) - D_0(S-Cl) - E_{\text{int}}(Cl(^2P_J)) - E_T, \quad (1)$$

where $E_{h\nu}$ is the energy of the photon used for photodissociation, 147.8 kcal/mol. We assume that the parent molecules are rotationally cooled and have a thermal distribution of vibrational energy at the nozzle temperature, 298 K. The average internal energy of the precursor, $E_{\text{int}}(CH_3SO_2Cl)$, is 1.8 kcal/mol using the vibrational frequencies calculated at the CCSD(T)/6-311++G(2*df*,*p*) level. The S–Cl bond energy, $D_0(S-Cl)$, at the CCSD(T)/aug-cc-pV(Q+d)Z//CCSD(T)/6-311++G(2*df*,*p*) level, including the core-valence correlation, relativistic, and atomic Cl spin-orbit corrections, is 65.6 kcal/mol. The internal energies in each Cl spin-orbit state, $Cl(^2P_{3/2})$ and $Cl(^2P_{1/2})$, are 0 and 2.52 kcal/mol, respectively. Because it is difficult to decompose the $P(E_T)$ obtained from the detection of stable radicals into its two contributions, radicals that were formed in conjunction with $Cl(^2P_{3/2})$ and those formed in conjunction with $Cl(^2P_{1/2})$, we superimpose the total internal energy of nascent radicals+Cl from the scattering experiment on the critical points of the potential energy surface calculated at the CCSD(T)/aug-cc-pV(Q+d)Z//CCSD(T)/6-311++G(2*df*,*p*) level in Fig. 9. The figure also shows, in dashed line, the internal energy distribution for stable radicals+Cl obtained from this work. At low internal energy, the distributions are essentially identical as these radicals do not have sufficient internal energy to dissociate. At higher internal energies the radical distribution falls off due to unimolecular dissociation. Having determined 70 kcal/mol as the threshold kinetic energy in Fig. 8, the experimentally determined barrier height from Eq. (1) for methylsulfonyl radical dissociation to CH_3+SO_2 is 14 ± 2 kcal/mol.

From the data shown in Fig. 3, we know the relative contribution of $CH_3SO_2+Cl(^2P_{3/2})$ and $CH_3SO_2+Cl(^2P_{1/2})$ at each recoil translational energy. In the high recoil translational energy region, between 50 and 80 kcal/mol, the shape of the $P(E_T)$ for these two pathways is nearly identical. By integrating the area under the curves in this energy range, we find ~63% of the total $P(E_T)$ is from $CH_3SO_2+Cl(^2P_{1/2})$ and ~37% is from $CH_3SO_2+Cl(^2P_{3/2})$. We use these percentages to decompose the total recoil kinetic energy distribution of the ground state radicals measured in the scattering experiment into its two contributions, the ones momentum matched to $Cl(^2P_{1/2})$ and the others momentum matched to $Cl(^2P_{3/2})$. Using Eq. (1), we calculate the internal energy distribution of nascent radicals for each of these kinetic energy distributions. The radicals formed in conjunction with $Cl(^2P_{1/2})$ have 2.52 kcal/mol less internal energy than those formed with $Cl(^2P_{3/2})$. Figure 10 shows the resulting total $P(E_{\text{int}}(CH_3SO_2))$. We note that the assumption that the peaks are identical in shape is very good at recoil kinetic energies below 70 kcal/mol. However, the $P(E_T)$ for CH_3SO_2 radicals+$Cl(^2P_{3/2})$ contributes ~50%, not 37%, to the total $P(E_T)$ at kinetic energies above 70 kcal/mol, so the $P(E_{\text{int}}(CH_3SO_2))$ is slightly overestimated at internal energies below 14 kcal/mol.

E. Detection of CH_3 radicals

With 118 nm photoionization, we also detected CH_3 radicals [ionization potential of 9.84 eV (Ref. 34)]. The CH_3^+ ion image is shown in Fig. 11. The small background from

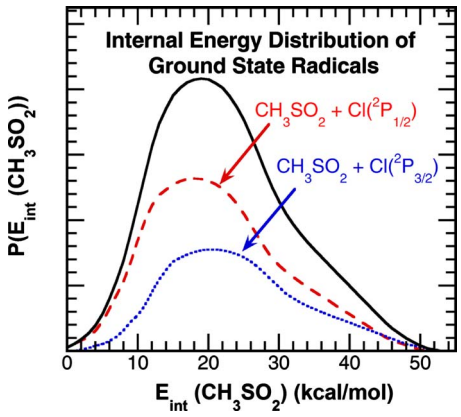

FIG. 10. The internal energy distribution of nascent radicals formed in the ground electronic state (solid line) calculated from the long dashed line $P(E_T)$ shown in Fig. 3 of the following paper and the $Cl(^2P_{3/2}):Cl(^2P_{1/2})$ ratio measured in this imaging data. This total $P(E_{int}(CH_3SO_2))$ is a sum of the internal energy distributions of radicals which have momentum-matched cofragment $Cl(^2P_{3/2})$ (dotted line) and $Cl(^2P_{1/2})$ (dashed line).

193 nm only and 118 nm only was subtracted in the data analysis (details in EPAPS supplement, Fig. S.11). CH_3 radicals are formed in three reaction channels: photolysis resulting in primary $S-CH_3$ bond fission, secondary dissociation of ground state CH_3SO_2 radicals, and secondary dissociation of CH_3SO_2 radicals formed in electronically excited states ($1\ ^2A''$, $2\ ^2A''$). It is unlikely that any CH_3^+ ions result from daughter fragmentation of CH_3SO_2Cl or stable CH_3SO_2 at the low photoionization energy used, 10.5 eV. The methyl product speed distribution in Fig. 12, derived from the image in Fig. 11, is broad and extends to 4000 m/s. One can accurately predict the speed distribution of the methyl radicals from secondary dissociation from CH_3SO_2 from the measured speed distribution of the momentum-matched SO_2 radicals. This is done in the following paper (we did not detect SO_2 in the imaging experiments because its IE is greater than 12 eV), but even the simple analysis below indicates that a primary $S-CH_3$ bond fission channel is the source of the highest velocity methyl products evident in Fig. 12.

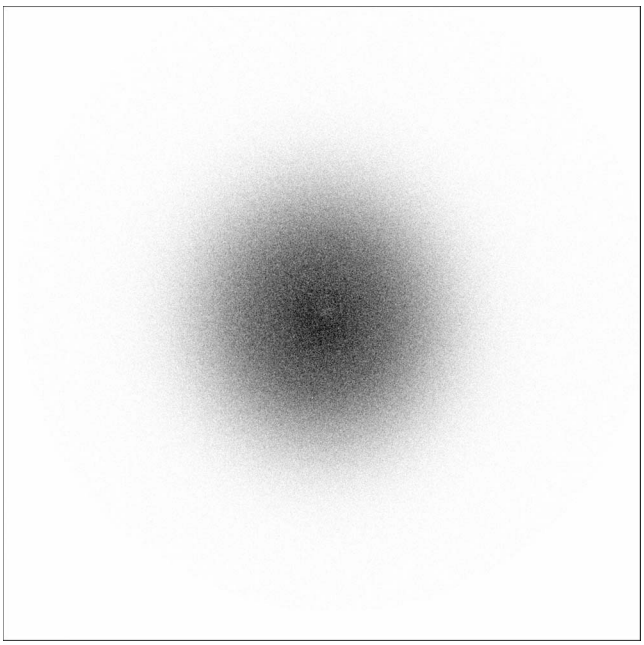

FIG. 11. Raw image of CH_3 obtained from 193 nm photodissociation and 118 nm photoionization. The 193 nm beam is polarized in the plane perpendicular to the detector. The repeller voltage was 4000 V and the extractor voltage was 2848 V. The image depicted is 901×901 pixels.

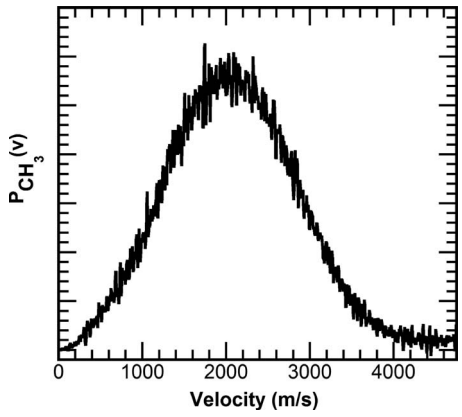

FIG. 12. Speed distribution for the observed CH_3 radicals. CH_3 radicals are formed in three channels: $CH_3SO_2Cl+h\nu \rightarrow CH_3+SO_2Cl$, $CH_3SO_2(X\ ^2A') \rightarrow CH_3+SO_2$, $CH_3SO_2(1\ ^2A'', 2\ ^2A'') \rightarrow CH_3+SO_2$.

For nascent radicals formed in the ground state, an average of 65 kcal/mol is partitioned into recoil kinetic energy in the primary photodissociation and an average of 0.9 kcal/mol is partitioned into recoil kinetic energy in the subsequent secondary dissociation channel [determined from the $P(E_T)$ reported for this channel in the following paper]. If the CH_3 fragments recoil in the forward direction, the highest observed velocity of CH_3 radicals from this secondary channel would be ~ 2100 m/s. For methyl products from the dissociation of nascent radicals formed in electronically excited states, the speed distribution of these methyl fragments is predicted to be broader but slower on average. This is because the velocities of these methyl products result from adding the slower primary recoil velocity of CH_3SO_2 to the higher kinetic energy recoil of CH_3 from SO_2 (dissociation on the repulsive regions of the radical's excited states imparts more energy to relative kinetic energy than the ground state dissociation). The appearance of a significant number of CH_3 radicals above these speeds indicates that the fastest CH_3 radicals result from primary $S-CH_3$ bond fission during 193 nm photodissociation. The following paper distinguishes between the CH_3 products from the two secondary dissociation channels by detecting the momentum-matched cofragments, SO_2. The remaining methyl radical signal allows us to determine a $P(E_T)$ for the minor primary photodissociation channel of the photolytic precursor, $S-CH_3$ photofission, shown in Fig. 10 of the following paper.

F. Dynamics of methylsulfonyl chloride photodissociation

Since the photodissociation laser was linearly polarized for the ion images of Cl in Fig. 2, these images also provide information about the angular distribution of the methylsulfonyl chloride photofragments. The $Cl(^2P_{3/2})$ angular distribution is fitted using the equation

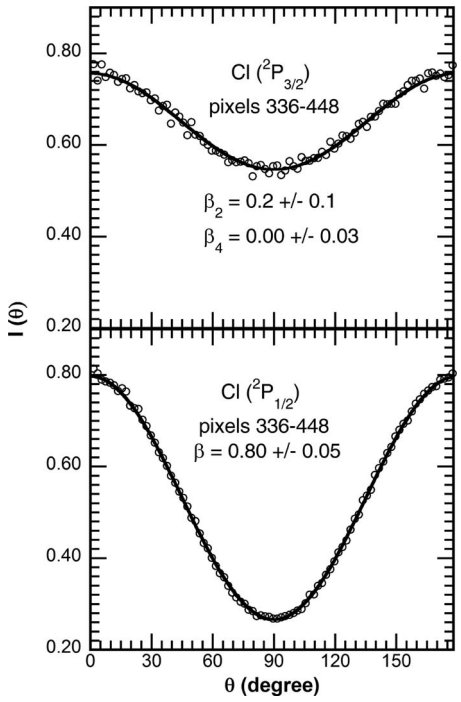

FIG. 13. Angular distributions for $Cl(^2P_{3/2})$ and $Cl(^2P_{1/2})$ detected 336–448 pixels from the center of the ion image. This corresponds roughly to vertical recoil kinetic energies between 45 and 80 kcal/mol, which is the photodissociation channel for producing ground electronic state CH_3SO_2+Cl.

$$I(\theta) \propto 1 + \beta_2 P_2(\cos\theta) + \beta_4 P_4(\cos\theta) \quad (2)$$

because the signal depends both on the anisotropy of the photodissociation process and on the REMPI detection of the $J=3/2$ atoms. The $Cl(^2P_{1/2})$ angular distribution is fitted with

$$I(\theta) \propto 1 + \beta P_2(\cos\theta), \quad (3)$$

where θ is the angle between the recoiling fragment's velocity vector and the electric vector of the photolysis laser and β is the anisotropy parameter. P_2 is the second-order Legendre polynomial and P_4 is the fourth-order Legendre polynomial.

We examine the anisotropy of the kinetic energy ranges that correspond roughly to photodissociation events that resulted in ground electronic state and excited electronic state radicals. The signal appearing in the Cl images in the range of 336–448 pixels from the center of the image corresponds to a recoil kinetic energy range (for vertically recoiling fragments) of 45–80 kcal/mol. This is the range in which ground electronic state radicals are formed. In this range, the $\beta_2 = 0.23 \pm 0.08$ and $\beta_4 = 0.00 \pm 0.02$ for $Cl(^2P_{3/2})$ and $\beta = 0.80 \pm 0.03$ for $Cl(^2P_{1/2})$, as shown in Fig. 13. Weighting these anisotropies by each channel's relative contribution to the total $P(E_T)$ in this kinetic energy range gives an anisotropy of $\beta = 0.59 \pm 0.08$. This averaged anisotropy parameter is in good agreement with that determined in the following paper ($\beta = 0.47-0.65$), but the large difference between the anisotropy parameters for the $Cl(^2P_{3/2})$ channel and the $Cl(^2P_{1/2})$ channel reveals that at least two electronic excited states may be accessed upon 193 nm photoexcitation of CH_3SO_2Cl.

Crude CIS(D) calculations reveal three singlet excited states with vertical excitation energies predicted in the range of 6.3–7.0 eV. The results from these calculations are summarized in Table III. The two lowest-lying singlet states are the $1\ ^1A''$ ($n_{O,Cl}$ of a'' symmetry $\rightarrow \sigma^*_{S\text{-}Cl}$ of a' symmetry) and $2\ ^1A'$ ($n_{O,Cl}$ of a' symmetry $\rightarrow \sigma^*_{S\text{-}Cl}$ of a' symmetry) states with symmetry determined with respect to the plane containing the C, S, and Cl atoms. These two singlet states have transition dipole moments perpendicular to the S-Cl bond and both oscillator strengths are 0.002. The third singlet state, $3\ ^1A'$ (a' orbital of mixed σ_{S-Cl}, σ_{S-C}, and n_O character $\rightarrow \sigma^*_{S-Cl}$ of a' symmetry), has a transition dipole moment that is parallel to the S–Cl bond and an oscillator strength of 0.32. The orbitals involved in the electronic transitions to these low-lying excited states are shown in Fig. 14. Clearly, the $CH_3SO_2(\tilde{X}) + Cl(^2P_{3/2})$ and $CH_3SO_2(\tilde{X}) + Cl(^2P_{1/2})$ products come from initial excitation of CH_3SO_2Cl to at least two of these excited states, one with a parallel transition dipole moment and one with a perpendicular transition dipole moment. The observed angular distribution of the $CH_3SO_2(\tilde{X}) + Cl(^2P_{1/2})$ products indicates they are predominantly from initial excitation to the $3\ ^1A'$ excited electronic state of CH_3SO_2Cl.

The signal appearing in the Cl images in the range of 0–316 pixels from the center of the image corresponds to a vertical recoil kinetic energy range of 0–40 kcal/mol. This is the range in which radicals in excited electronic states are produced. In this lower kinetic energy range, $Cl(^2P_{3/2})$ atoms recoil with anisotropy $\beta_2 = 0.60 \pm 0.02$ and $\beta_4 = 0.00 \pm 0.02$, while $Cl(^2P_{1/2})$ atoms have $\beta = 0.51 \pm 0.06$, Fig. 15. Weighting these anisotropies by their relative contribution to the total $P(E_T)$ in this kinetic energy range gives an anisotropy of $\beta = 0.59 \pm 0.06$. These anisotropy parameters confirm previous results, indicating that the dissociation of methylsulfonyl chloride is prompt relative to molecular rotation and that the transition dipole moment is predominantly parallel.

TABLE III. CIS(D) calculations of the CH_3SO_2Cl excited states.

	CIS(D) energy (eV)	Oscillator strength	Transition dipole moment[a]			Angle with S–Cl bond	Prompt axial recoil β
			x	y	z		
$1\ ^1A''$	6.34	0.002	0	0	−0.1169	90°	−1.0
$2\ ^1A'$	6.88	0.002	−0.0145	−0.1105	0	100°	−0.9
$3\ ^1A'$	7.06	0.32	−1.2198	0.215	0	167°	1.8

[a]The CH_3SO_2Cl molecule is oriented so that the vector along the S–Cl bond is (0.9986, 0.0528, 0) and the carbon, sulfur, and chlorine atoms lie in the x,y plane.

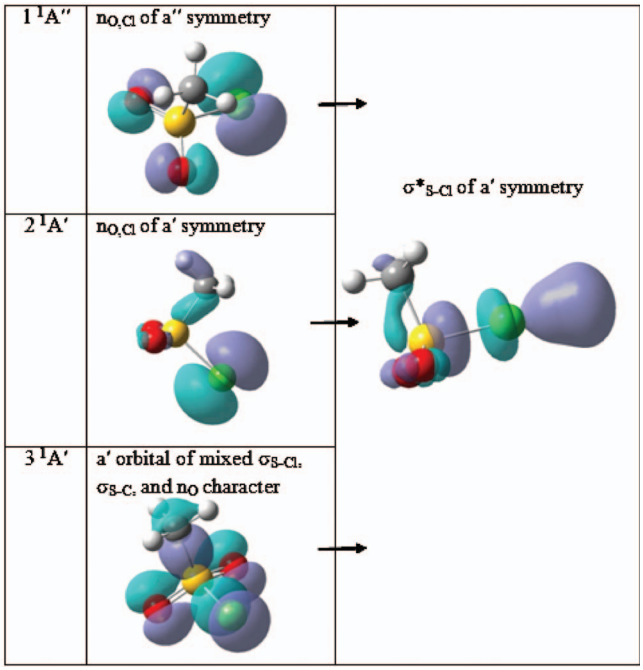

FIG. 14. The orbitals involved in electronic transitions to low-lying excited states of CH_3SO_2Cl. We depict only the orbitals for the dominant electronic configuration contributing to each excited electronic state in the Franck–Condon region.

V. DISCUSSION

The photodissociation of CH_3SO_2Cl at 193 nm primarily results in S–Cl bond fission to create ground and excited electronic state CH_3SO_2 radicals momentum matched to Cl, with an angular distribution characterized by $\beta=0.59$.

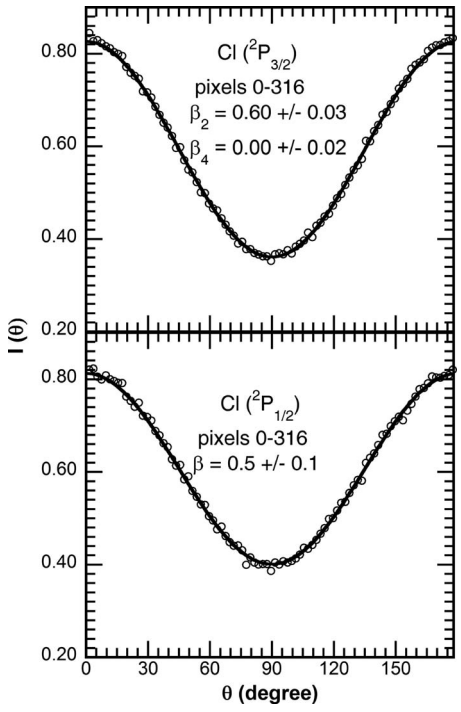

FIG. 15. Angular distributions for $Cl(^2P_{3/2})$ and $Cl(^2P_{1/2})$ detected 0–316 pixels from the center of the ion image. This corresponds roughly to vertical recoil kinetic energies between 0 and 40 kcal/mol, which is the photodissociation channel for producing electronically excited CH_3SO_2 radicals+Cl.

CIS(D) calculations suggest that the measured angular distribution reflects initial excitation of the CH_3SO_2Cl precursor to more than one excited state, with differing orientations of the transition dipole moment with respect to the breaking S–Cl bond. To help define the exact energy partitioning to internal energy in the CH_3SO_2 radicals produced in the ground electronic state, we determine the spin-orbit branching ratio of the Cl atom cofragments. Using energy conservation, we determine the internal energy distribution of nascent $CH_3SO_2(\tilde{X})$ radicals. Some of these radicals are formed with internal energy above the barrier for dissociation to CH_3+SO_2, so measuring the velocity distribution of the remaining stable radicals at $m/e=79$, $CH_3SO_2^+$, allows us to experimentally determine the energy of the dissociation barrier. This determination relies on a calculated $D_0(S-Cl)$ of the photolytic precursor which we take as the CCSD(T) value of 65.6 kcal/mol. Using this bond energy, the experimental onset for dissociation of the radicals determines the barrier height for dissociation to CH_3+SO_2 to be 14 ± 2 kcal/mol. As mentioned previously, our CCSD(T) theoretical prediction to this barrier height is at the CCSD(T)/aug-cc-pV(Q+d)Z level and includes ZPVE, core-valence correlation, and relativistic effects. Using the smaller of the available basis in the correlation-consistent basis set series, the convergence of the predicted barrier height is 0.9 kcal/mol, and thus our present prediction on the forward barrier height for $CH_3SO_2\rightarrow CH_3+SO_2$ has an uncertainty of at least 0.9 kcal/mol. Nevertheless, the experimentally determined barrier height is in excellent agreement with the theoretically predicted one of 14.6 kcal/mol. Our CCSD(T) results also suggest that the tight *d*-augmented correlation-consistent basis sets are good for predicting TS energies for chemical reactions involving sulfur-containing radicals.

The total internal energy distribution of the nascent CH_3SO_2 radicals determined from this work is drastically different than that assumed by Owrutsky *et al.* It is bimodal, indicating that both ground and excited electronic state CH_3SO_2 radicals are formed. Our measured internal energy distribution shows that 22% of the radicals formed in the ground electronic state have internal energy below the experimentally determined dissociation barrier. In contrast, the radicals detected in Owrutsky *et al.*'s time-resolved photoionization experiments showed $<2\%$ remaining radicals after 2 ps. Thus, it is clear that those experiments were probing the decay of electronically excited radicals.

While the present experiments definitively benchmark the high-level CCSD(T) prediction of the dissociation barrier for $CH_3SO_2\rightarrow CH_3+SO_2$, one is also interested in how the dissociation rate changes with internal energy across a predetermined internal energy distribution. Using femtosecond time-resolved velocity map imaging, one could measure this change in rate with internal energy for the ground state radicals characterized here and distinguish them from the electronically excited radicals. Time-resolved imaging experiments by Shibata *et al.*[35] have measured the dissociation rate of acetyl radicals produced from the photodissociation of acetyl chloride. By monitoring the decay of signal in the outermost regions of the image with time, the decay rate of

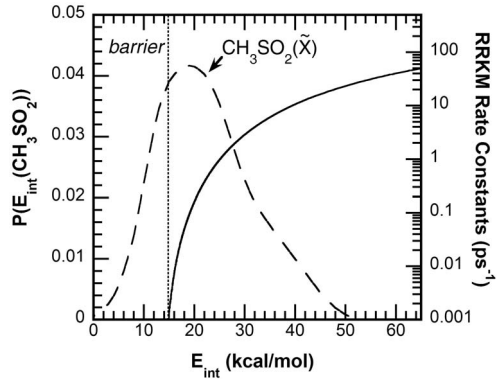

FIG. 16. Internal energy distribution of the ground electronic state CH_3SO_2 radicals (also shown in Fig. 10), the CCSD(T) asymptotic barrier, and RRKM dissociation rate constants at low rotational energy ($T=1$ K). For nearly the entire internal energy range, we use the microcanonical rates calculated from the $R_{C-S}=2.6$ Å intermediate TS, Fig. S.12. For internal energies within 0.2 kcal/mol of the asymptotic barrier, the calculations use the microcanonical rates calculated from the structure at $R_{C-S}=4$ Å, also presented in Fig S.12.

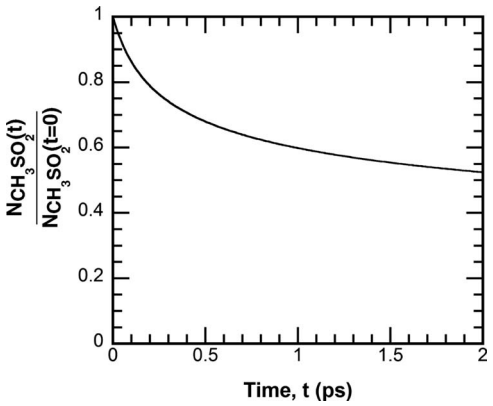

FIG. 17. We predict the overall decay of ground electronic state CH_3SO_2 radicals using the internal energy distribution and RRKM rate constants shown in Fig. 16. Approximately 22% of the ground state radicals will not dissociate as they have internal energies below the barrier.

$CH_3SO_2(\tilde{X})$ radicals in Fig. 4 could be determined without interference from the dissociation dynamics of the excited state radicals. Our CCSD(T) results allow us to predict the outcome of such a temporally and spatially resolved experiments. We describe these predictions below.

For simple bond fission reactions occurring via a loose TS, one should use variational TS theory to predict the energy dependence of the microcanonical dissociation rate constant. In the CH_3SO_2 system, however, there is an intermediate barrier along the C–S bond reaction coordinate that serves as a bottleneck for the reactive flux so a variational calculation may not be necessary. To crudely assess the range of energies for which the intermediate TS at $R_{C-S}=2.6$ Å serves as a bottleneck, we computed the microcanonical rates using both this structure and a looser structure at $R_{C-S}=4$ Å along the reaction coordinate (the EPAPS supplement gives the geometry and vibrational frequencies for the 4 Å structure). As shown in Fig S.12 of the EPAPS supplement, we find that the microcanonical rates using the intermediate TS become smaller than those using the 4 Å structure within 0.2 kcal/mol of the asymptotic barrier energy. Figure 16 shows the normalized internal energy distribution of the ground electronic state CH_3SO_2 radicals from this work and the RRKM rate constants $k(E_{int})$ calculated[36] assuming the rotational energy of the radical is low ($T=1$ K). Because our experiments do not determine the energy partitioning between vibration and rotation in the radical, we also investigated the sensitivity of the microcanonical rates to rotational energy. As the C–S bond stretches, a portion of the energy in the two-dimensional (2D) adiabatic rotor is released to active energy in the RRKM calculation, $\Delta E_J = E_J^{\dagger} - E_J = (1 - I_{zD}^{\dagger}/I_{zD})E_J^{\dagger}$, where I_{2D} is the 2D adiabatic moment of inertia which conserves the angular momentum quantum number J when the molecules are approximated as symmetric tops. The 298 K microcanonical rate constants are given in the EPAPS supplement, Fig. S.13; they are only slightly smaller than those given in Fig. 16. Thus, the microcanonical rate constants shown in Fig. 16 offer a crude prediction for what might be measured in a time and spatially resolved femtosecond imaging experiment of CH_3SO_2 unimolecular dissociation.

Using the RRKM reaction rates presented in Fig. 16, which were calculated assuming rotationally cold ground electronic state radicals and our ground electronic state CH_3SO_2 internal energy distribution shown in Fig. 10, we predict the decay rate of ground electronic state CH_3SO_2 radicals that would be observed in a femtosecond time-resolved experiment that does not resolve the radicals by internal energy. The overall decay is shown in Fig. 17, with the fraction of surviving radicals at time t given by

$$\frac{N(t)}{N(t=0)} = \sum_{E_{int}} P(E_{int}) e^{(-k(E_{int})\cdot t)} \Delta E. \quad (4)$$

(We use $\Delta E=1$ kcal/mol.) Further analysis assuming an instrument time resolution of 350 fs, similar to the experiment of Owrutsky *et al.*, is presented in the EPAPS supplement, Fig. S.14. As anticipated, the overall decay predicted for the ground state CH_3SO_2 radicals is much slower than that measured in the ultrafast photoionization experiments of Owrutsky *et al.*

The results presented in this paper also bear on prior bulk kinetics studies of the atmospheric oxidation of dimethyl sulfide. Ravishankara *et al.* suggested that adducts such as CH_3SO_2 play a critical role in the temperature dependence of the [methanesulfonic acid]/$[SO_4^{2-}]$ ratio. As their study used an early endothermicity of 17.2 kcal/mol for the reaction barrier, the value of 14 kcal/mol presented here better defines the temperature dependence of the unimolecular dissociation rate constants of CH_3SO_2 in the overall kinetic mechanism. Using the intermediate TS between the radical and loosely bound complex as a bottleneck for unimolecular dissociation, our calculated[36,37] high-pressure rate constants at temperatures between 180 and 320 K are shown in Fig. 18. Although the assumption of a harmonic density of states for the molecule leads to dramatic errors in the absolute rate constants, the temperature dependence shown in Fig. 18 is still informative. The magnitude of our calculated high-pressure thermal rate constants increases by a factor of 6 when going from 200 to 210 K and a factor of 189 when

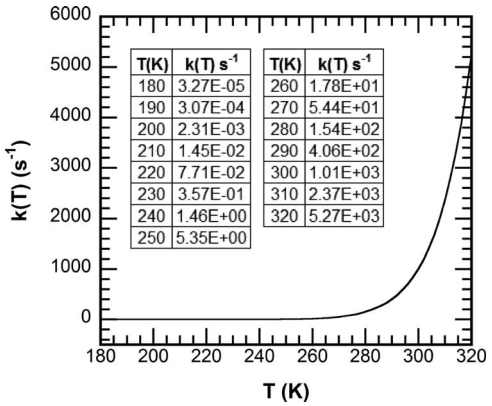

FIG. 18. High-pressure, thermal rate constants for $CH_3SO_2 \rightarrow CH_3+SO_2$. Although these calculated absolute rate constants are overestimated because we assume harmonic vibrational partition functions, the ratios of rates at different temperatures are more robust.

going from 250 to 300 K. In contrast, the assumed Arrhenius expression for CH_3SO_2 dissociation in the model used by Ravishankara *et al.* gives unimolecular dissociation rates that differ by a factor of 7.9 when the temperature changes from 200 to 210 K and a factor of 321 when going from 250 to 300 K. Although our calculated thermal high-pressure rate constants change less steeply with temperature than those from the approximate expression used by Ravishankara *et al.*, the variation in temperature is still marked. Thus the conclusion of Ravishankara *et al.*, that adducts such as CH_3SO_2 play a critical role in the observed $[MSA]/[SO_4^{2-}]$ temperature dependence, is still reasonable.

We end with one caution in the modeling of the temperature dependence of the CH_3SO_2 dissociation in atmospheric models. Although, our high-pressure rate constant at 300 K of 1.0×10^3 s^{-1} compares favorably with the high-pressure rate constant of 2×10^3 s^{-1} calculated by Le Bras and coworkers, CH_3SO_2 in the atmosphere is formed from exothermic reactions such as CH_3SO+NO_2. Thus, the nascent CH_3SO_2 molecules in the atmosphere are not thermally at equilibrium and the observed unimolecular dissociation rates may differ from those obtained in the high-pressure limit.

ACKNOWLEDGMENTS

The experimental work herein was supported by the National Science Foundation (Grant No. CHE-0746050) (L.J.B.) and the Donors of the American Chemical Society Petroleum Research Fund (Grant No. 47480-AC6) (L.J.B.). The CCSD(T) computational results presented here were supported by a grant from the Research Grants Council of the Hong Kong Special Administrative Region, China (Project No. CityU 101507) (K.-C.L.). K.-C.L. acknowledges the preliminary work by Min-Yang Tsang to explore the potential energy surface for the isomerizations and dissociations of CH_3SO_2 radical at the City University of Hong Kong. We also thank John Barker and Lam Nguyen for their help using the MULTIWELL suite of programs. B.J.R. acknowledges support from a NSF Graduate Research Fellowship.

[1] S. B. Barone, A. A. Turnipseed, and A. R. Ravishankara, Faraday Discuss. **100**, 39 (1995).
[2] K.–C. Lau, Y. Liu, and L. J. Butler, J. Chem. Phys. **123**, 054322 (2005).
[3] X. N. Tang, B. J. Ratliff, B. L. FitzPatrick, and L. J. Butler, J. Phys. Chem. B **112**, 16058 (2008).
[4] L. Zhu and J. W. Bozzelli, J. Mol. Struct.: THEOCHEM **728**, 147 (2005).
[5] J. M. L. Martin, J. Chem. Phys. **108**, 2791 (1998).
[6] J. M. L. Martin, Chem. Phys. Lett. **310**, 271 (1999).
[7] T. H. Dunning, Jr., K. A. Peterson, and A. K. Wilson, J. Chem. Phys. **114**, 9244 (2001).
[8] A. K. Wilson and T. H. Dunning, Jr., J. Chem. Phys. **119**, 11712 (2003).
[9] A. K. Wilson and T. H. Dunning, Jr., J. Phys. Chem. A **108**, 3129 (2004).
[10] R. D. Bell and A. K. Wilson, Chem. Phys. Lett. **394**, 105 (2004).
[11] N. X. Wang and A. K. Wilson, J. Phys. Chem. A **109**, 7187 (2005).
[12] D. Borissenko, A. Kukui, G. Laverdet, and G. Le Bras, J. Phys. Chem. A **107**, 1155 (2003).
[13] A. Kukui, V. Bossoutrot, G. Laverdet, and G. Le Bras, J. Phys. Chem. A **104**, 935 (2000).
[14] A. Ray, I. Vassalli, G. Laverdet, and G. Le Bras, J. Phys. Chem. **100**, 8895 (1996) and earlier references within.
[15] A. J. Frank and F. Turecek, J. Phys. Chem. A **103**, 5348 (1999).
[16] J. C. Owrutsky, H. H. Nelson, and A. P. Baronavski, J. Phys. Chem. A **105**, 1440 (2001).
[17] B. W. Alligood, B. L. FitzPatrick, E. J. Glassman, L. J. Butler, and K.-C. Lau, J. Chem. Phys. **131**, 044305 (2009).
[18] A. J. R. Heck and D. W. Chandler, Annu. Rev. Phys. Chem. **46**, 335 (1995).
[19] A. T. J. B. Eppink and D. H. Parker, Rev. Sci. Instrum. **68**, 3477 (1997).
[20] Y. Sato, Y. Matsumi, M. Kawasaki, K. Tsukiyama, and R. Bersohn, J. Phys. Chem. **99**, 16307 (1995).
[21] Y. Liu and L. J. Butler, J. Chem. Phys. **121**, 11016 (2004).
[22] Note that most authors label the upper state for detection of $Cl(^2P_{1/2})$ as the $4p\ ^2P_{1/2}$ state from C. E. Moore, NSRDS-NBS 35, 1 (1971); however, the NIST Atomic Spectra Database has adopted the reassignment of this upper state at 85 917.937 cm^{-1} to a ^2S state, as recommended in the comprehensive reanalysis of the chlorine spectrum by L. J. Radziemski, Jr. and V. Kaufman, J. Opt. Soc. Am. **59**, 424 (1969). (To avoid confusion, we give the original C. E. Moore assignment here. For the energy of the transition, we use the NIST value of 85 917.937–882.3515 cm^{-1}.)
[23] B. Chang, R. C. Hoetzlein, J. A. Mueller, J. D. Geiser, and P. L. Houston, Rev. Sci. Instrum. **69**, 1665 (1998).
[24] C. Hampel, K. A. Peterson, and H. Werner, Chem. Phys. Lett. **190**, 1 (1992); M. J. O. Deegan and P. J. Knowles, *ibid.* **227**, 321 (1994); P. J. Knowles, C. Hampel, and H. J. Werner, J. Chem. Phys. **99**, 5219 (1993).
[25] T. H. Dunning, Jr., J. Chem. Phys. **90**, 1007 (1989).
[26] K. A. Peterson and T. H. Dunning, Jr., J. Chem. Phys. **117**, 10548 (2002).
[27] W. A. de Jong, R. J. Harrison, and D. A. Dixon, J. Chem. Phys. **114**, 48 (2001); M. Douglas and N. M. Kroll, Ann. Phys. **82**, 89 (1974).
[28] H.-J. Werner, P. J. Knowles, R. Lindh, F. R. Manby, M. Schütz, P. Celani, T. Korona, G. Rauhut, R. D. Amos, A. Bernhardsson, A. Berning, D. L. Cooper, M. J. O. Deegan, A. J. Dobbyn, F. Eckert, C. Hampel, G. Hetzer, A. W. Lloyd, S. J. McNicholas, W. Meyer, M. E. Mura, A. Nicklaß, P. Palmieri, R. Pitzer, U. Schumann, H. Stoll, A. J. Stone, R. Tarroni, and T. Thorsteinsson, MOLPRO is a package of *ab initio* programs.
[29] C. E. Moore, *Atomic Energy Levels*, Natl. Bur. Stand. (U.S.) Circ. No. 467 (U.S. GPO, Washingtons, D.C., 1949).
[30] See EPAPS supplementary material at http://dx.doi.org/10.1063/1.3159556 for energies, geometries, and rotational constants of the intermediates and transition states for the CH_3SO_2 potential energy surface calculated at the CCSD(T) level of theory. Also found in the supplementary material are some experimental data and rate constant calculations not included in the manuscript.
[31] M. J. Frisch, G. W. Trucks, H. B. Schlegel *et al.*, GAUSSIAN 03, Revision E.01, Gaussian, Inc., Wallingford CT, 2004.
[32] V. Dribinski, A. Ossadtchi, V. A. Mandelshtam, and H. Reisler, Rev. Sci. Instrum. **73**, 2634 (2002).
[33] R. Liyanage, Y. A. Yang, S. Hashimoto, R. J. Gordon, and R. W. Field, J.

Chem. Phys. **103**, 6811 (1995).
[34] J. Berkowitz, G. B. Ellison, and D. Gutman, J. Phys. Chem. **98**, 2744 (1994).
[35] T. Shibata, H. Li, H. Katayanagi, and T. Suzuki, J. Phys. Chem. A **102**, 3643 (1998).
[36] MULTIWELL-2009.2 software, May 2009, designed and maintained by J. R. Barker with contributors N. F. Ortiz, J. M. Preses, L. L. Lohr, A. Maranzana, P. J. Stimac, and L. T. Nguyen, University of Michigan, Ann Arbor, MI, http://aoss.engin.umich.edu/multiwell/; J. R. Barker, Int. J. Chem. Kinet. **33**, 232 (2001).
[37] See Eq. 3.21 in K. A. Holbrook, M. J. Pilling, and S. H. Robertson, *Unimolecular Reactions*, 2nd ed. (Wiley, Chichester, 1996).